THE EUROPEAN PHYSICAL JOURNAL PLUS

Regular Article



Inferring lateral tension distribution in wall structures of single cells

Danush Chelladurai¹, Giulia Galotto², Jocelyn Petitto³, Luis Vidali^{2,4}, Min Wu^{4,5,a}

- Massachusetts Academy of Math and Science, Worcester, MA 01605, USA
- ² Biology and Biotechnology, Worcester Polytechnic Institute, Worcester, MA 01605, USA
- ³ WPI UMASS Medical School Joint PhD Program, Worcester Polytechnic Institute, Worcester, MA 01605, USA
- ⁴ Bioinformatics and Computational Biology, Worcester Polytechnic Institute, Worcester, MA 01605, USA
- ⁵ Mathematical Sciences, Worcester Polytechnic Institute, Worcester, MA 01605, USA

Received: 20 May 2020 / Accepted: 3 August 2020 / Published online: 17 August 2020 © Società Italiana di Fisica and Springer-Verlag GmbH Germany, part of Springer Nature 2020

Abstract We present an inference scheme that maps relative lateral tensions along the cell wall based on the cell outline coordinates. The full tension-inference approach presented here includes the primary scheme that maps the tension distributions on the discretized cell outlines and their optimizations to smooth polynomials. We have studied the stability of the primary scheme against small noise analytically and have shown that the scheme is more stable to noise when discretization of the cell outline is coarser. We have found agreement quantitatively between the error bounds predicted by the analysis and the error computed from numerical experiments, when the scheme is applied to synthetic cell outlines from a computational model of hyper-elastic thin-shell deformation. Then, we develop an optimization method that effectively restores the spatial resolution of the primary scheme by converting the discrete tension distributions to smooth polynomials. In the end, we apply the full scheme to map tension distributions in moss protonemal cells.

1 Introduction

Varying mechanical properties influence the emergent growth and morphogenesis of living organisms. As such, many efforts are made to understand their forms by studying how tissues actively generate stresses and respond to these stresses both mechanically and chemically. In single cells, with and without a cell wall enclosure, their characteristic length and morphology are regulated differently. While actomyosin-induced stretches and osmotic pressure can deform animal cells easily, the architecture and integrity of plant, fungi, and bacteria cells are maintained by the cell wall structure, which provide support against mechanical stresses. Hence, the advancing knowledge of stress and mechanical property distribution in the cell wall improves our understanding of growth and morphogenesis in wall-cell organisms.

As for wall structures of single cells, multiple approaches have been developed to map the stresses [1–7]. Since many single cell structures take a quasi-axially symmetric shape, and their thickness is much smaller than the size of the cell, the majority consider only the in-plane



^a e-mail: englier@gmail.com (corresponding author)

tensile stresses, or alternatively the lateral tensions which are the in-plane tensile stresses multiplied by the cell-wall thickness along the meridional and circumferential directions [1– 5], while a few consider the full possible mechanical interaction (e.g., bending [6,7] and shear stresses [8]). When only the lateral tensions are considered in counterbalancing the turgor pressure, one can map the relative tension distributions from reconstructing the curvatures from the image data, as has been done in [5,9,10]. However, when errors are introduced to the reconstructed cell outline during imaging recording and processing, it is a challenge to reconstruct curvatures reliably. It is unknown how this inference scheme responds to noise, and thus, the reliability of the inferred lateral tensions is not clear. As a result, many groups still rely on full biomechanical models with extra material property assumptions to map the tension distributions by simulations (e.g., [4,11])

In this paper, we present an inference scheme that maps lateral tensions along the cell wall based on the cell outline coordinates. The full tension-inference approach presented in this study includes the primary scheme that map the tension distributions on the discretized cell outlines and their approximated polynomial representation. We have studied the stability of the primary scheme against small noise analytically and have found agreement between the error bounds predicted by the analysis and the error computed from numerical experiments when the scheme is applied to synthetic cell outlines from a computational model of hyper-elastic thin-shell deformation. In the end, we apply the full scheme to map tension distributions in moss protonemal cells (see Fig. 1).

The paper is organized as follows. In Sect. 2, we provide the background of the geometry and mechanics in axially symmetric cell walls. In Sect. 3, we formulate the basic inference scheme that computes the tensions as step-function distributions based on the cell outline coordinates and perform sensitivity analysis to this scheme. In particular, we provide a formula of how small cell outline perturbation propagates to meridional and circumferential tensions. In Sect. 4, we apply the scheme to infer the tension distributions from cell outlines generated by a computational model. We show the relative error between the inferred tensions, and the simulated tensions agree within the error bound distribution predicted by the sensitivity analysis. In Sect. 5, we formulate an optimization scheme that converts the primary step-function tensions to smooth polynomial distributions. In Sect. 6, we apply the full inference scheme to map tensions in moss protonema. We discuss our results in tensions

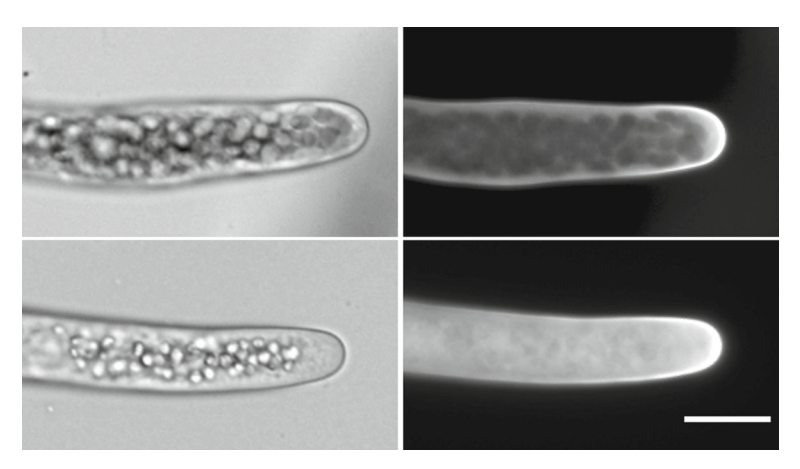


Fig. 1 Representative chloronema (top panels) and caulonema (low panels) cells. Left, bright field pictures; right, fluorescent image of cell wall stained with calcofluor-white. Scale bar $20\,\mu m$



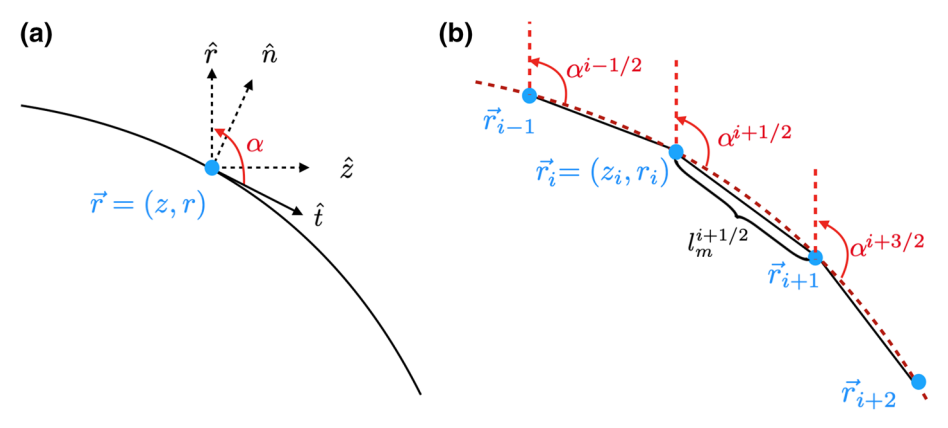


Fig. 2 a Schematic of the cell wall represented by the curve $\vec{r}(s) = (r(s), z(s))$ where s is the arc length from a reference point. **b** The cell wall is represented by a list of markers $\vec{r}_i = (r_i, z_i)$. The length and angle of the linear segment between \vec{r}_i and \vec{r}_{i+1} are denoted by $l_m^{i+1/2}$ and $\alpha^{i+1/2}$, respectively

with their connections to the material property and growth on the cell wall and conclude in Sect. 7.

2 Geometry and mechanics along the cell wall

Given the thickness of the cell wall is much thinner than its observed radii of curvatures, we describe its thin-shell wall structure as a surface of revolution. The shape of the cell wall is represented by the curve $\vec{r}(s) = (z(s), r(s))$, where z is the coordinate along the axis of symmetry, r is the local distance from the axis of symmetry (i.e., local cell width), and s is the arc length from a reference point. See Fig. 2. We further define α to be the angle from the local tangent \hat{r} , in the direction of increasing s, to the r-axis $(0 \le \alpha \le \pi)$. That is,

$$\hat{t} = \cos \alpha \times \hat{r} + \sin \alpha \times \hat{z}. \tag{1}$$

Similarly, we have the local outward normal of the cell wall

$$\hat{n} = \sin \alpha \times \hat{r} - \cos \alpha \times \hat{z}. \tag{2}$$

Then, we define the curvature along the meridional direction to be $\kappa_s = -\hat{n} \cdot d\hat{t}/ds$ (so it is positive at the tip), and from Eqs. (1) and (2), we have

$$\kappa_s = \mathrm{d}\alpha/\mathrm{d}s. \tag{3}$$

Similarly, the circumferential curvature is given by $\kappa_{\theta} = -\hat{n} \cdot d\hat{\theta}/ds_r$ where $\hat{\theta}$ is the unit vector along the direction orthogonal to \hat{n} and \hat{t} , ds_r is the incremental displacement along $\hat{\theta}$, and $d\hat{\theta}/ds_r = -\hat{r}/r$. Thus, we have

$$\kappa_{\theta} = \sin \alpha / r.$$
(4)

Accounting for the force balance $\nabla_s \cdot \boldsymbol{\sigma} + P\hat{n} = 0$ between the turgor pressure P and lateral tensions $\boldsymbol{\sigma}(s) = \sigma_s \hat{t} \otimes \hat{t} + \sigma_\theta \hat{\theta} \otimes \hat{\theta}$ for axially symmetric surfaces [12], we can derive

$$d(\sigma_s \hat{t})/ds + (\sigma_s - \sigma_\theta)\hat{r}/r + (-\sigma_s \sin \alpha/r + P)\hat{n} = 0.$$
 (5)



 σ_s and σ_θ are the tension pair along the meridional and the circumferential direction, respectively. They are in-plane meridional and circumferential stresses multiplied by the cell wall thickness, respectively.

While Eq. (5) gives the algebraic equation

$$\kappa_s \sigma_s + \kappa_\theta \sigma_\theta = P,\tag{6}$$

between tensions along \hat{n} -direction, it gives the differential equation $\partial(\sigma_s \sin \alpha)/\partial r = P$ $(\sigma_s \sin \alpha)/r$ along \hat{z} -direction. We can find $\sigma_s \sin \alpha = Pr/2$ as its solution. Taking this together with Eq. (4), we have

$$\kappa_{\theta} \sigma_{s} = P/2.$$
(7)

Equations (6) and (7) connecting tensions and the turgor pressure lead to

$$\sigma_{s} = P/(2\kappa_{\theta}) \tag{8}$$

$$\sigma_{\theta} = P/(2\kappa_{\theta}) \times (2 - \kappa_{s}/\kappa_{\theta}). \tag{9}$$

Given Eqs. (8) and (9), one can infer the local tensions σ_s and σ_{θ} relative to turgor pressure P based on the local curvatures κ_s and κ_{θ} , as has been done in [5,9,10]. Below, we present our tension inference scheme based on the assumption $P \neq 0$ and is a constant along the cell outline.

3 Tension inference scheme

We discretize the cell outline curves by N+1 marker points $\vec{r}_i = (z_i, r_i), i = 1, 2, \dots, N+1$, connected by N linear segments. See Fig. 2 for one cell outline and its discretization. On each linear segment $\Box^{i+1/2}$, $i=1,2,\ldots,N$, we compute its angle $\alpha^{i+1/2}$, length $l_m^{i+1/2}$, and the averaged local distance from the axis of symmetry (i.e., local cell width), $r_m^{i+1/2}$, by

$$\alpha^{i+1/2} = \arctan[(z_{i+1} - z_i)/(r_{i+1} - r_i)]$$
(10)

$$l_m^{i+1/2} = |\vec{r}_{i+1} - \vec{r}_i|$$

$$r_m^{i+1/2} = (r_i + r_{i+1})/2.$$
(11)

$$r_m^{i+1/2} = (r_i + r_{i+1})/2. (12)$$

Reconstructing the meridional curvature on the non-boundary linear segments (i = $2, 3, \ldots, N-1$) by $\kappa_s^{i+1/2} = [\mathrm{d}\alpha/\mathrm{d}s]^{i+1/2} \approx [\overline{\alpha}_{i+1} - \overline{\alpha}_i]/l_m^{i+1/2}$ in finite difference of the angles averaged on the marker points $\overline{\alpha}_i = (\alpha^{i-1/2} + \alpha^{i+1/2})/2$ and $\overline{\alpha}_{i+1} = (\alpha^{i-1/2} + \alpha^{i+1/2})/2$ $(\alpha^{i+1/2} + \alpha^{i+3/2})/2$, we derive

$$\kappa_s^{i+1/2} = (\alpha^{i+3/2} - \alpha^{i-1/2})/(2l_m^{i+1/2}).$$
(13)

On the two boundary linear segments $\Box^{1+1/2}$ and $\Box^{N+1/2}$, we define $\alpha^{1-1/2} = \pi - \alpha^{1+1/2}$ and $\alpha^{N+3/2}=2\pi-\alpha^{N+1/2}$ and still use Eq. (13) to approximate $\kappa_s^{1+1/2}$ and $\kappa_s^{N+1/2}$. We reconstruct the circumferential curvature on all the linear segments $\Box^{i+1/2}$ $(i=1,2,\ldots,N)$ by

$$\kappa_{\theta}^{i+1/2} = \sin \alpha^{i+1/2} / r_m^{i+1/2}. \tag{14}$$

Based on the reconstructed curvatures, we can infer tensions between the markers by

$$\sigma_s^{i+1/2} = P/(2\kappa_\theta^{i+1/2}) \tag{15}$$



$$\sigma_{\theta}^{i+1/2} = \sigma_s^{i+1/2} (2 - \kappa_s^{i+1/2} / \kappa_{\theta}^{i+1/2}). \tag{16}$$

Although walled cells do not fluctuate as much as animal cells, the perturbation to the actual cell outline may arise in the imaging recording, processing, and the cell outline reconstruction. How sensitive is the inferred tensions to the inaccuracy of the cell marker positions? To quantify the stability of the result against local perturbations of cell marker positions, we consider the effect of an arbitrary small perturbation in cell marker positions $(\delta z_i, \delta r_i)$'s and compute the resulted relative perturbations on the local inferred tensions $(\delta \sigma_s/\sigma_s)^{i+1/2}$ and $(\delta \sigma_\theta/\sigma_\theta)^{i+1/2}$ through Eqs. (10)–(16):

$$\left(\frac{\delta\sigma_s}{\sigma_s}\right)^{i+1/2} = -\left(\frac{\delta\kappa_\theta}{\kappa_\theta}\right)^{i+1/2} \tag{17}$$

$$\left(\frac{\delta\sigma_{\theta}}{\sigma_{\theta}}\right)^{i+1/2} = -\left(\frac{2(1-\beta)}{2-\beta}\frac{\delta\kappa_{\theta}}{\kappa_{\theta}} + \frac{\beta}{2-\beta}\frac{\delta\kappa_{s}}{\kappa_{s}}\right)^{i+1/2}$$
(18)

where $\beta = \kappa_s/\kappa_\theta$ and

$$\left(\frac{\delta \kappa_s}{\kappa_s}\right)^{i+1/2} = \frac{\delta \alpha^{i+3/2} - \delta \alpha^{i-1/2}}{\alpha^{i+3/2} - \alpha^{i-1/2}} - \left(\frac{\delta l_m}{l_m}\right)^{i+1/2} \tag{19}$$

$$\left(\frac{\delta \kappa_{\theta}}{\kappa_{\theta}}\right)^{i+1/2} = \frac{\delta \alpha^{i+1/2}}{\tan \alpha^{i+1/2}} - \left(\frac{\delta r_m}{r_m}\right)^{i+1/2} \tag{20}$$

where

$$\delta \alpha^{i+1/2} = \frac{\tan \alpha^{i+1/2}}{1 + (\tan \alpha^{i+1/2})^2} \left(\frac{\delta z^{i+1} - \delta z^i}{z^{i+1} - z^i} - \frac{\delta r^{i+1} - \delta r^i}{r^{i+1} - r^i} \right)$$
(21)

$$\delta l_m^{i+1/2} = \sin \alpha^{i+1/2} (\delta z^{i+1} - \delta z^i) + \cos \alpha^{i+1/2} (\delta r^{i+1} - \delta r^i)$$
 (22)

$$\delta r_m^{i+1/2} = (\delta r^{i+1} + \delta r^i)/2. \tag{23}$$

From the above perturbation analysis, we can see the effect of location on the sensitivity of the tensions. From Eqs. (17), (18) and (20), we show the inferred tensions are most sensitive to the perturbation at the tip region with $\tan \alpha^{i+1/2} \to 0$ and $r_m^{i+1/2} \to 0$. We can also see the effect of local curvatures on the sensitivity of the circumferential tension. From Eq. (18) alone, we show at locations where $\beta = \kappa_s/\kappa_\theta \to 2$, tension inferences along the circumferential direction are unstable to small perturbations. Finally, we can see that the sensitivity of both tensions is affected by the discretization resolution of the cell outline. From Eqs. (17), (18), (19), and (21), we show the inferred tensions are more sensitive to the local perturbation everywhere as marker points are closer along z- and r-axis, respectively, when $(z^{i+1}-z^i) \to 0$, $(r^{i+1}-r^i) \to 0$. This observation makes a counterintuitive point that when the discretization is finer (coarser), the inference scheme is less (more) stable to noise.

Although the locally inferred tensions from Eqs. (10)–(16) do not require equidistant discretization of the cell outline, in the following results, we discretize the cell outlines equidistantly along the arc length where the discretization resolution can be controlled globally. Note that the value of the turgor P does not affect the sensitivity analysis Eqs. (17)–(23). In this paper, we assume P = 1, which is equivalent to inferring the tensions rescaled by the turgor pressure magnitude. If P is given in practice, one can multiply the relative tensions by the value of P.

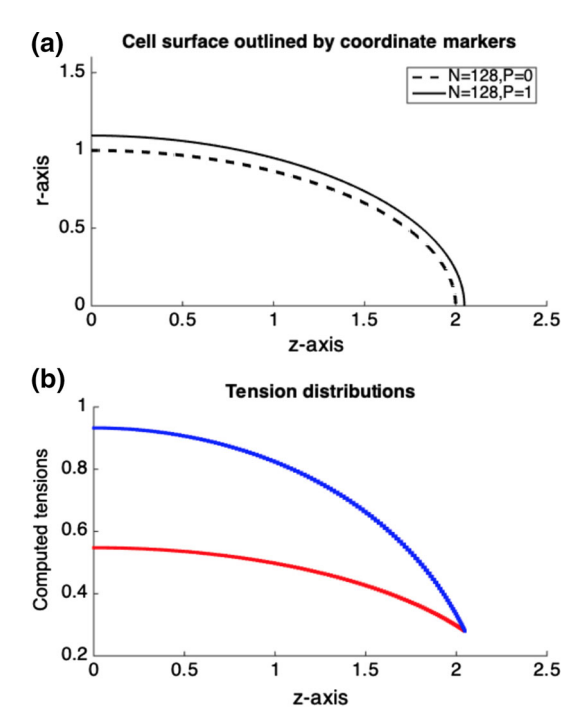


4 Inferring tensions from synthetic data

To test the accuracy of the inference scheme, especially in the presence of noise, we generate synthetic data of cell outlines from a simple mechanical model (see "Appendix A" for details). Figure 3a shows an example of a cell outline simulated from deforming a half-ellipsoid $r^2 + z^2/4 = 1$ by the turgor pressure P = 1. Figure 3b shows the meridional and circumferential tension distributions along the N = 128 linear segment from the simulation, where the circumferential tension is larger than the meridional tensions everywhere except at the tip. Both tensions decrease as approaching the tip. We apply the inference scheme with both low resolution (using $N_I = 16$ linear segments) and high resolution (using $N_I = 128$ linear segments) and find the inferred tensions agree well with the simulated tensions in both low and high resolution with below 10% and 2.5% relative error, respectively, throughout the cell outline (see Fig. 4). Thus, the precision is improved when the resolution is higher. However, our perturbation analysis has suggested that the high-resolution inference may not be the best choice in practice due to noise.

To show this, we add noise to the computed cell outline by perturbing the coordinates \vec{r}_i 's with small displacements drawn from a uniform distribution $U(-\delta_m/2, \delta_m/2)$ in both $z_i \rightarrow z_i + U(-\delta_m/2, \delta_m/2)$ and $r_i \rightarrow r_i + U(-\delta_m/2, \delta_m/2)$ independently, where δ_m is defined as the displacement noise. We first investigate the behavior of high-resolution inference with $N_I = 128$. For very small $\delta_m = 0.01\%$ × the cell maximal width, both inferred meridional and circumferential tensions are close enough to the simulated ones (see Fig. 5, top). Interestingly, the meridional tension inferences are more accurate than the circumferential ones. We will show later this observation is quantitatively consistent with the perturbation analysis. As we increase $\delta_m = 0.1\%$ × the cell maximal width, inferred

Fig. 3 a Simulated cell outlines without (dashed lines) and with (solid lines) turgor pressure. **b** Meridional (red) and circumferential (blue) tensions from the simulation. The *z*- and *r*-axes are rescaled by the cell maximal width without turgor pressure





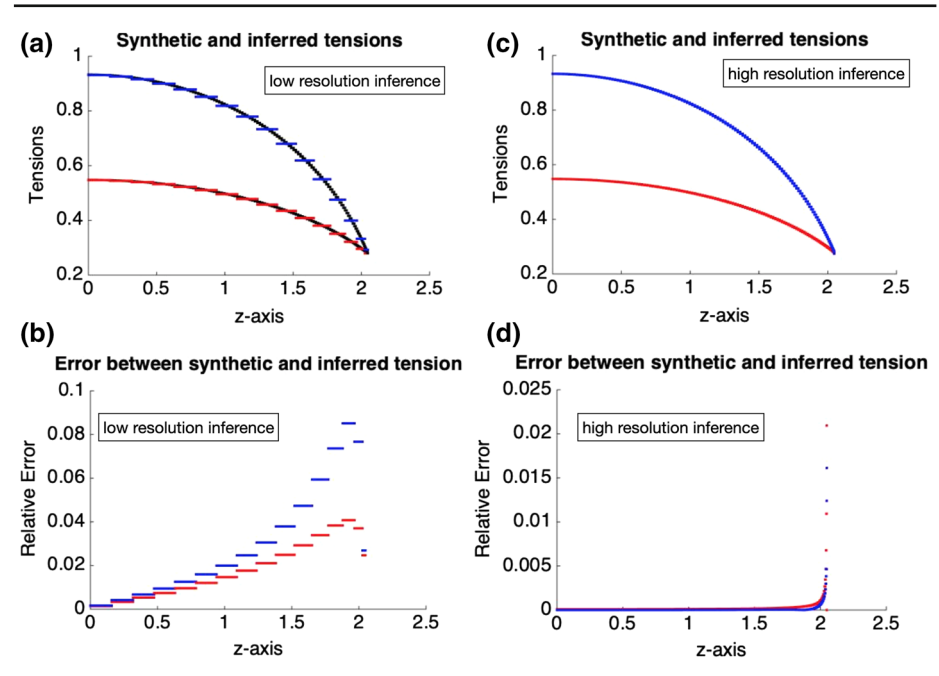


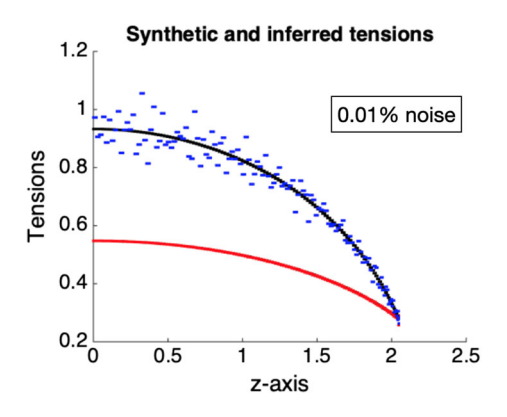
Fig. 4 Inferred meridional tensions (red) and circumferential tensions (blue) as step functions versus synthetic tensions from the simulation (black). For the low-resolution inference (a), we use the number of linear segments $N_I = 16$ to compare with the computed tension distribution from the simulation using N = 128. We show that the relative errors in both meridional and circumferential tensions are below 0.1 (b). For the high-resolution inference (c), we use the same number of linear segments $N_I = 128$ as that used in the simulation N = 128. We show that the relative error in both meridional and circumferential tensions is below 0.025 (d). Note in c, synthetic tensions from the simulation are overlapped by the inferred meridional tensions (red) and circumferential tensions (blue). The z-axis is rescaled by the cell maximal width without turgor pressure. Turgor pressure P = 1 is assumed to infer the relative tensions

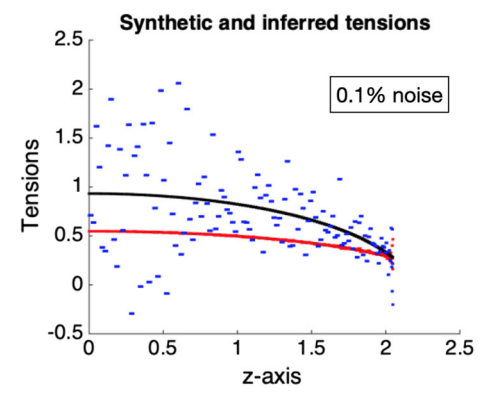
tensions are no longer close to the simulated ones using $N_I = 128$ linear segments (see Fig. 5, bottom).

The perturbation analysis predicts that inferred tensions are more sensitive to the perturbation as marker points are closer. This means decreasing the number of linear segments N_I in inferring the same cell outline improves the stability of the scheme to the noise. Indeed, we show with $\delta_m = 0.1\%$ × the cell maximal width, and application of the inference scheme with $N_I = 64$ is able to generate reliable inferences with relative error below 0.5. See Fig. 6a–c. As we further increase $\delta_m = 1\%$ × the cell maximal width, we have to decrease $N_I = 16$ to generate reliable inferences with relative error below 0.5. See Fig. 6d–f. Notice in Fig. 6b, c and e, f, we have also plotted the upper bound of the relative errors (see the black step functions) predicted by perturbation analysis. The numerical relative errors are indeed bounded by the theoretical bounds. Thus, we have quantitatively validated our perturbation analysis. Notice the prediction made by the analysis that the inferred meridional tension has a larger sensitivity to the local perturbation at the tip region is also validated (See Fig. 6b, e). In summary, we show theoretically and numerically that this inference scheme is more robust to noise when the discretization is coarser. However, when the discretization becomes coarse, the resolution of the inferred tension is limited by the step-function representation.



Fig. 5 Inferred meridional tensions (red) and circumferential tensions (blue) versus tensions from the simulation (black) with 0.01% noise (top) and 0.1% noise (bottom). The inferred meridional tensions (red) are very accurate and almost overlap with the simulated meridional tension. For both cases, we use the same number of linear segments $N_I = 128$ as that used in the simulation N = 128. Note synthetic meridional tensions from the simulation are overlapped by the inferred meridional tensions (red). The z-axis is rescaled by the cell maximal width without turgor pressure. Turgor pressure P = 1is assumed to infer the relative tensions





5 Optimizing the primary inference scheme

To improve the step-function representation of the tension distribution with N linear segments, and to better use multiple data samples, we convert the step functions into a polynomial by degree $n_p \le N - 1$:

$$P(z) = \sum_{i=0}^{n_p} a_i z^i$$
 (24)

where the coefficients a_i 's are obtained by minimizing the sum of the squared integral $\sum_{h=1}^{M} \int_{s_h} (f_h(s) - P(s))^2 ds$ along the cell outline s_h , over M data samples, which gives

$$\phi = \sum_{h=1}^{M} \int_{a_h}^{b_h} (f_h(z) - P(z))^2 W_h(z) dz$$
 (25)

where a_h and b_h are lower and upper bounds of z and $W_h(z) = ds/dz = 1/\sin(\alpha(z))$ for the hth cell outline. Then, we expand $\phi\left(a_0,\ldots,a_{n_p}\right)$ into



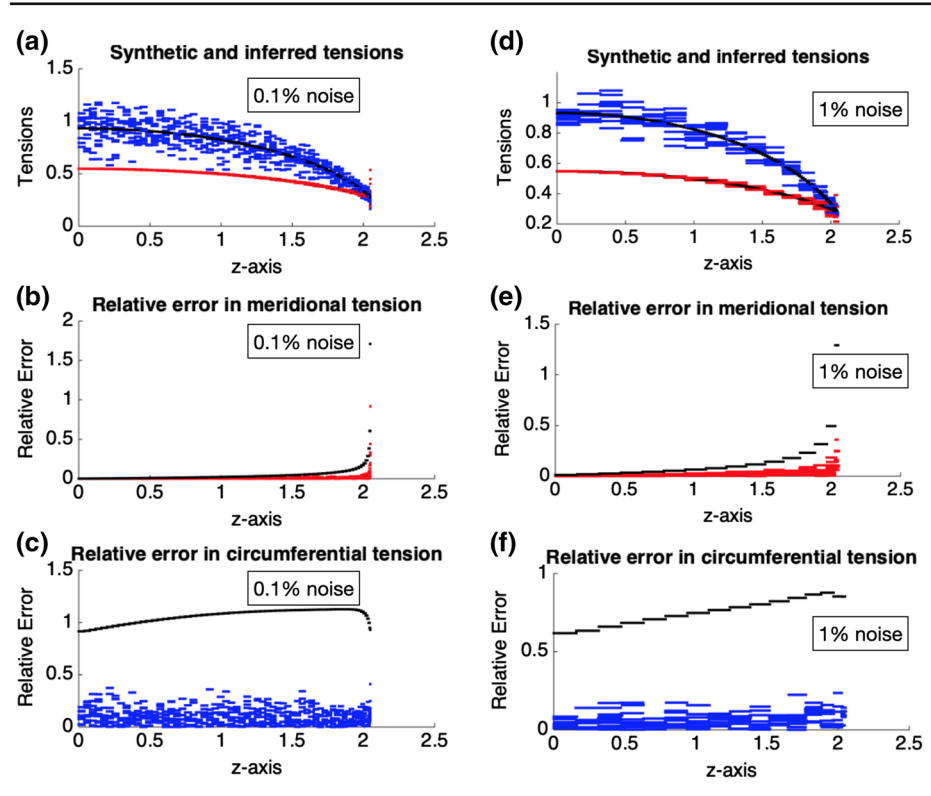


Fig. 6 Inferred tension distributions as step functions along linear segments. With ten synthetic image data generated by perturbing the simulated marker-point coordinates within $0.1\% \times (\text{cell width})$ in displacement, we infer tension distributions by discretizing the cell outlines by $N_I = 64$ linear segments (\mathbf{a} - \mathbf{c}). We show that the inference scheme is more stable in the meridional tension, as shown in red step functions in \mathbf{a} and \mathbf{b} . The circumferential tensions are more sensitive to perturbations, as shown in blue step functions in \mathbf{a} and \mathbf{d} . The relative errors from the perturbed synthetic data are below the error bounds from the perturbation analysis, as shown in black step functions in \mathbf{b} and \mathbf{c} . For a larger perturbation of $1\% \times (\text{cell width})$ in displacement, as guided by the perturbation analysis, we have inferred tension distributions by discretizing the cell outlines by a lower number of $N_I = 16$ linear segments (\mathbf{d}) and have achieved comparable relative errors (\mathbf{e} - \mathbf{f}) (meridional data in red and circumferential data in blue). The z-axis is rescaled by the cell maximal width without turgor pressure. Turgor pressure P = 1 is assumed to infer the relative tensions

$$\phi = \sum_{h=1}^{M} \int_{a_h}^{b_h} f_h^2(z) W_h(z) dz - 2 \sum_{h=1}^{M} \sum_{i=0}^{n_p} a_i \int_{a_h}^{b_h} z^i f_h(z) W_h(z) dz + \sum_{h=1}^{M} \sum_{i=0}^{n_p} \sum_{j=0}^{n_p} a_i a_j \int_{a_h}^{b_h} z^{i+j} W_h(z) dz.$$

To minimize ϕ , we have

$$0 = \frac{\partial \phi}{\partial a_k} = -2 \sum_{h=1}^{M} \int_{a_h}^{b_h} z^k f_h(z) W_h(z) dz + \sum_{h=1}^{M} \sum_{i=0}^{n_p} a_i \int_{a_h}^{b_h} z^{i+k} W_h(z) dz + \sum_{h=1}^{M} \sum_{i=0}^{n_p} a_j \int_{a_h}^{b_h} z^{j+k} W_h(z) dz$$



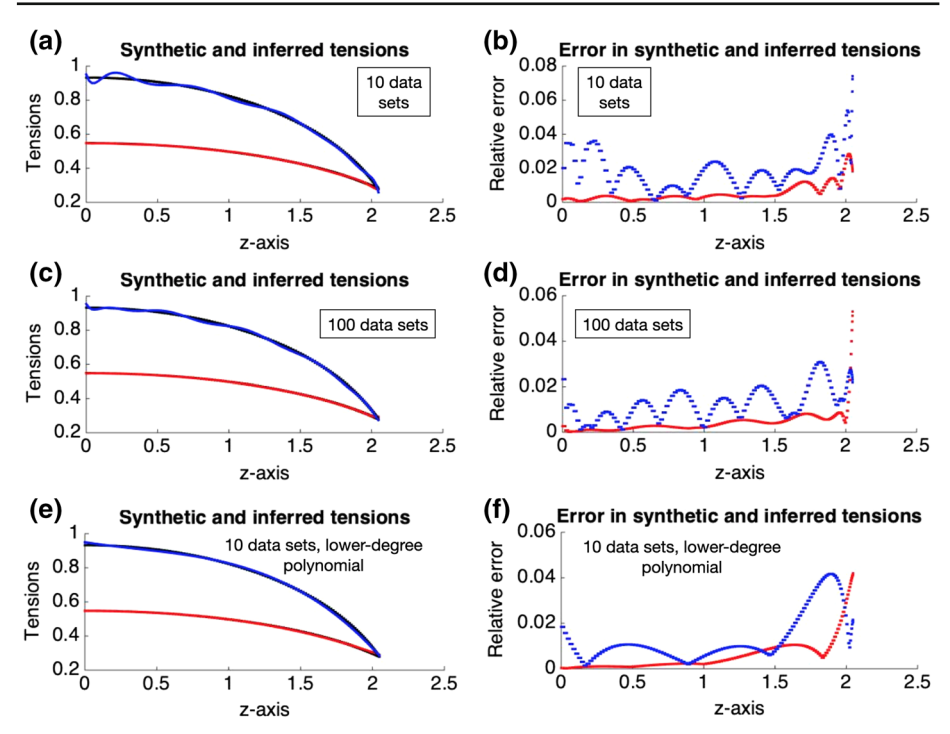


Fig. 7 Inferred tension distributions as polynomial functions. (Meridional data in red and circumferential data in blue.) Using the inferred step-function tensions from 100 synthetic image data with N=16 linear segments, a $n_p=15$ th degree polynomial is constructed from the least square integral problems (a). See text for details of the method. The relative errors for both tensions are within 8% (b). By increasing the number of synthetic noisy samples to 100 (c, d), the tension is less oscillatory in amplitude (c), and the relative errors are further reduced everywhere except the tip region (d). By reducing the degree of the polynomial to be $n_p=3$ (c), we can reduce the oscillation both in amplitude and wavenumber (f). The z-axis is rescaled by the cell maximal width without turgor pressure. Turgor pressure P=1 is assumed to infer the relative tensions

for $k = 0, 1, ..., n_p$. As such, we obtain the normal equation system to solve $a = (a_0, ..., a_{n_p})^T$ from Ha = c where

$$H_{ij} = \sum_{h=1}^{M} \int_{a_h}^{b_h} z^{i+j} W_h(z) dz \quad \text{and} \quad c_i = \sum_{h=1}^{M} \int_{a_h}^{b_h} z^i f_h(z) W_h(z) dz$$
 (26)

for $i=0,1,\ldots,n_p$ and $j=0,1,\ldots,n_p$. To show the effectiveness of this optimization method, we generate ten data samples by perturbing the simulated cell outline in Fig. 3 within 1% cell width in displacement, and for each data sample, we use the primary tension inference scheme from Sect. 4 with N=16 to generate the step-function tension distributions. Then, we apply the optimization method with $n_p=N-1=15$ to convert the tension distribution to the smooth distributions (see Fig. 7a). The inferred tensions closely oscillate around the simulated tension values along the cell outline, which can be seen more clearly from Fig. 7b, which shows the relative errors between the smoothed inferred tension and the simulated tension. Nevertheless, the errors in both tensions are overall smaller than the errors from the step-function inference (compare with Fig. 6e, f). The errors in circumferential tensions are still larger than the meridional ones almost everywhere, which echos the error behavior in the step-function inference (see Fig. 6e, f). We show the oscillatory errors can be reduced in



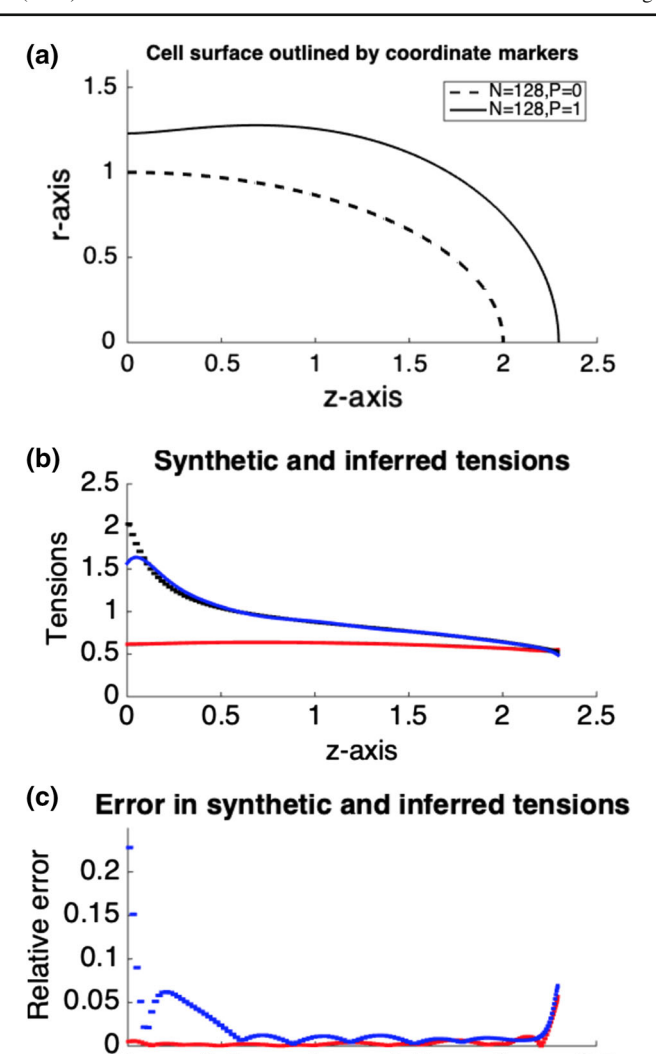


Fig. 8 a Simulated cell outlines with non-monotonic cell width along the z-axis (solid lines). This shape is generated by the same elliptical shape without turgor pressure (dashed line) and with a decrease the elastic moduli along z-direction when turgor pressure P=1 is applied. **b** Inferred meridional (red) and circumferential (blue) tensions against $1\% \times$ (cell width) displacement noise. The simulated tensions are marked in black. The inferred meridional tension overlaps with the simulated one. The inferred circumferential tension overlaps with the simulated one except near the rear boundary. The z-axis is rescaled by the cell maximal width without turgor pressure. Turgor pressure P=1 is assumed to infer the relative tensions

1.5

z-axis

2

0.5

the amplitude by introducing more data samples (Fig. 7c, d) and can be also reduced in both the amplitude and the wavenumber by decreasing n_p (see Fig. 7e, f when $n_p = 3$). However, the improvement in precision with both auxiliary approaches is not phenomenal.

To further test the effectiveness of our method, we have implemented the method with different cell outline shapes. See Fig. 8 for the inferred tension in comparison with the



simulated tension for a cell with non-monotone cell width along z-axis. We generate ten data samples by perturbing the simulated cell outline in Fig. 8 within 1% cell width (the maximal in r) in displacement, and we generate the polynomial using the ten step-function tension distributions with N=16. The overall relative error is below 5% except for the circumferential tension at near the rear boundary. At the rear boundary, due to the coarse discretization, the inferred circumferential tension is lower than the simulated tension when the tension is increasing drastically toward the boundary point.

6 Tension inference with moss data

At last, we apply the full inference scheme to infer the average tensions for two different types of moss protonemata, caulonemata, and chloronemata. We obtain 14 caulonema cell outlines and 16 chloronema cell outlines from one-week old moss tissue (See Fig. 9a, c for cell outlines and see "Appendix B" for details of experiment, image acquisition, and processing). We show that the tensions relative to turgor pressure in chloronemata is higher in both directions at all locations than those in caulonema. Our results show that the tension is maximal along the circumferential direction, which is in agreement with what has been found during the tip growth of *Chara rhizoid* [9] and pollen tubes [5]. However, in root hairs, it has been found that the circumferential tension can be smaller than the meridional tension near the tip [10]. In addition, we have found at the tip of both types of cells are with lower tension level than other locations, which is in contrast to what has been found in root hair [10], while in agreement with what has been found during the tip growth of Chara rhizoid [9] and pollen tube [5]. In [13], multiple species of single walled cells have been studied in connecting their geometrical phenotype to growth distribution. It will be interested to apply our method to single walled cells from multiple species and connect their geometrical phenotype to the mechanical phenotype and compare the mechanical phenotype across species.

7 Discussion and conclusion

These results on the moss image data, as well as the synthetic data, suggest that small changes in cell diameter can have a significant mechanical effect on the cell wall. Our results show that the cell walls bear more tension along the circumferential direction, and the tension along the circumferential direction is more sensitive to the positional perturbations. Interestingly, a recent study applying a theory-data combined approach shows the lateral wall stiffness robustly scales with the cell diameter [7]. In fact, feedback mechanisms from the stress to the material properties have long been proposed and have been under study for a long time [14–20]. The above points altogether indicate that cell diameter, or equivalently the cell circumferences, may be limited in a feedback system where larger circumferential growth causes larger circumferential tension and then induces circumferential stiffening and stop further circumferential expansion. This may be relevant to the overall function of chloronemata, because larger cells have the capacity for increased photosynthesis, and chloronemata contain larger and more abundant chloroplasts than caulonemata [21], suggesting a primary role of these cells in photosynthesis. Future analyses of the cell wall of chloronemata and caulonemata will clarify how the plant controls its diameter and if a limit reached by chloronemal cells exists.

Further comparing the relative tension distributions to the turgor pressure in caulonemata and chloronemata, we see that the minimum value for relative tension at the tip is larger in



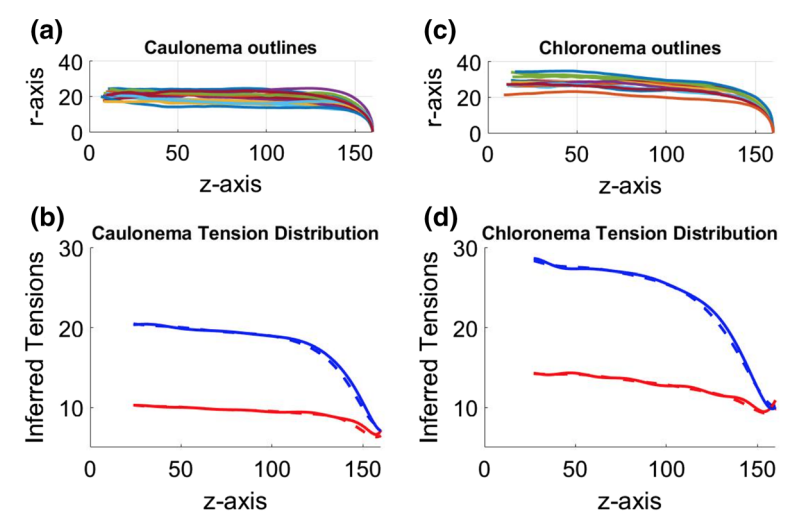


Fig. 9 a 14 caulonema outlines. **b** Inferred canonical meridional (red) and circumferential (blue) tensions of caulonema. **c** 16 chloronema outlines. **d** Inferred canonical meridional (red) and circumferential (blue) tensions of chloronemata. Chloronema has higher level of relative tensions to the turgor pressure. In **b** and **d**, the solid (dashed) lines are the tension inferences from using $N_I = 20$ ($N_I = 10$) linear segments and $n_p = 19$ th ($n_p = 9$ th) degree polynomial. For the $N_I = 20$ and $N_I = 10$ cases, each linear segment covers an arc length of 8 and 16 in pixel size along the cell wall, respectively. The *r*- and *z*-axes are rescaled by 0.315 μm. Turgor pressure P = 1 is assumed to infer the relative tensions

chloronemata. This may have implications for how fast these two cells can grow, consistent with the observation that growth rates are faster in caulonemata [22]. A prediction of this is that increasingly thinner cells may be able to withstand faster secretion and growth rates. For the tension distribution in caulonemata and chloronemata, we show here that the tip of both types of cells has a lower relative tension level than other locations. A site of low relative tension that coincides with active secretion may provide a buffer, where the material properties of the cell wall can be in flux. For example, while the cell requires increased extensibility at the tip to grow, the reduced tension should diminish the likelihood of the cell bursting in the process. Notice the range of turgor pressure has not been measured in chloronemata and caulonemata in this study or elsewhere to our knowledge. It has been measured in other systems such as in tip-growing pollen tubes from *Lilium longiflorum* using a pressure probe [23]. For *Lilium longiflorum*, the turgor pressure values ranged between 0.1 and 0.4 MPa. We will measure the turgor pressure in *Physcomitrella patens* protonemata in the future work. Then, the absolute tension values can be simply computed from relative tensions multiplied by the measured turgor pressure.

Although this simple image-based method based on Eqs. (8) and (9) has been applied in the previous work [5,9,10], the stability and limitations of this method have not been characterized in detail. In this work, we have addressed these two major difficulties and have further optimized the representation of inferred tensions from this method. The tension distribution is connected to both cell wall component deposition [2,24–28] and material property adaptations [1–4,7,20,29], as discussed above. Being able to map tensions independently from cell wall component deposition and material property adaptations can clear up the avenue to, in the future, systematically map tension distributions together with cell wall component deposition and material property adaptations.



Acknowledgements This work was in part supported by NSF Grant DMS-2012330 to M.W and MCB-1253444 to L.V.

Data availability statement This manuscript has associated data in a data repository. [Authors' comment: The code that is used in Fig. 9 and explained in Appendix B are available at https://github.com/DanukGOAT/Cell-Wall-Tension-Inference.]

8 Appendix A: A simple model of cell-wall mechanics

To test the accuracy of the inference scheme and its stability to small perturbations, we generate synthetic data by a simple mechanical model, where we combine the force balance Eq. (5) with a constitutive law between the lateral tensions and the lateral strains λ_s and λ_θ [30–32]:

$$\sigma_s = \frac{1}{2}\mu_h (1/(\lambda_\theta)^2 - 1/(\lambda_s)^2) + K_h(\lambda_s \lambda_\theta - 1)$$
 (27)

$$\sigma_{\theta} = \frac{1}{2}\mu_h(1/(\lambda_s)^2 - 1/(\lambda_{\theta})^2) + K_h(\lambda_s\lambda_{\theta} - 1). \tag{28}$$

This is equivalent to assuming the cell wall as a thin compressible neo-Hookean material where $\mu_h = h \times \mu$ and $K_h = h \times K$ are the rescaled shear and bulk modulus, respectively, as the multiplication between the local cell wall thickness h and shear modulus μ and the bulk modulus K, respectively. We can compute λ_s and λ_θ , respectively, by $\lambda_s = ds/ds^0$ and $\lambda_\theta = r/r^0$, where ds (ds^0) is the current (intrinsic) differential meridional arc length and r (r^0) is the current (intrinsic) radial distance from the z-axis. As shown in Fig. 2(b), we discretize the cell wall outline with linear segments between lattice-free marker points. By integrating Eq. (5) from the middle point ($z_m^{i-1/2}$, $r_m^{i-1/2}$) between (z_{i-1} , r_{i-1}) and (z_{i} , r_{i}), and the middle point ($z_m^{i+1/2}$, $r_m^{i+1/2}$) between (z_i , r_i) along the discretized outline, we obtain the approximated force balance equations

$$(\sigma_s \hat{t})^{i+1/2} - (\sigma_s \hat{t})^{i-1/2}$$

$$+ \ln\left(\frac{r_i}{r_m^{i-1/2}}\right) \left(\left[(\sigma_s - \sigma_\theta)\hat{r} - (\sigma_s \sin \alpha)\hat{n} \right] / \cos \alpha \right)^{i-1/2}$$

$$+ \ln\left(\frac{r_m^{i+1/2}}{r_i}\right) \left(\left[(\sigma_s - \sigma_\theta)\hat{r} - (\sigma_s \sin \alpha)\hat{n} \right] / \cos \alpha \right)^{i+1/2}$$

$$+ \frac{P}{2} \left((l_m \hat{n})^{i-1/2} + (l_m \hat{n})^{i+1/2} \right) = 0$$

$$(29)$$

on each marker point $2 \le i \le N$ between the tip and the rear boundary point. We index the rear boundary point by i = 1 and the tip point by i = N + 1. At the rear boundary, we assume the force balance along r-axis and fix its position along z-axis:

$$\ln\left(\frac{r_m^{1+1/2}}{r_1}\right) \left([(\sigma_s - \sigma_\theta) - (\sigma_s \sin^2 \alpha)] / \cos \alpha \right)^{1+1/2}$$

$$+ (\sigma_s \cos \alpha)^{1+1/2} + \frac{P}{2} (l_m \sin \alpha)^{1+1/2} = 0$$

$$z_1 = 0$$
(30)



and we implement $\sigma_s \sin \alpha = Pr/2$ at the tip segment N + 1/2 and fix the tip position along r-axis

$$(\sigma_s \sin \alpha)_{N+1/2} - Pr_{N+1/2}/2 = 0$$

$$r_{N+1} = 0$$
(32)

to close the system.

By approximating $\lambda_s^{i+1/2} = (ds/ds^0)^{i+1/2} \approx (l_m/l_m^0)^{i+1/2}$ and $\lambda_\theta^{i+1/2} = (r/r^0)^{i+1/2} \approx (r_m/r_m^0)^{i+1/2}$ on each linear segment, we can solve the cell outline by solving a nonlinear system of $\vec{r_i}$'s ($1 \le i \le N+1$) when $\vec{r_i}$ 0's are prescribed.

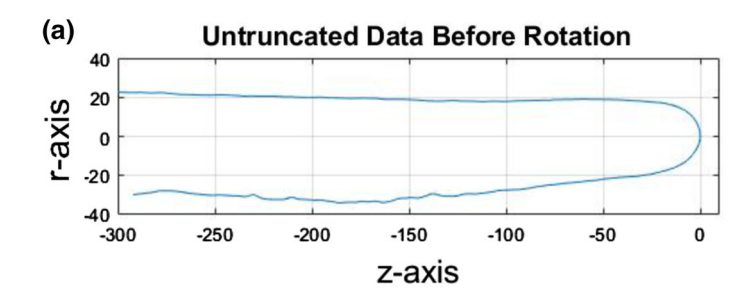
We have performed convergence test to various different cell outline initial configurations and have found the computed cell outline coordinates as well as the tension distributions all converge at least superlinearly as the number of the linear segments N increase. In Fig. 3a, we set the rescaled shear and bulk modulus to be constant, $\mu_h = 5$ and $K_h = 5$, respectively. In Fig. 8a, we set both $\mu_h(s^0)$ and $K_h(s^0)$ decreasing from 5 to 0.5 from the left rear end to the tip following the formula $x(s^0) = 5/(1+9 \times s^0/L)$. Without turgor pressure, L is the total arc length of the cell outline and s^0 is the arc length from the rear boundary point.

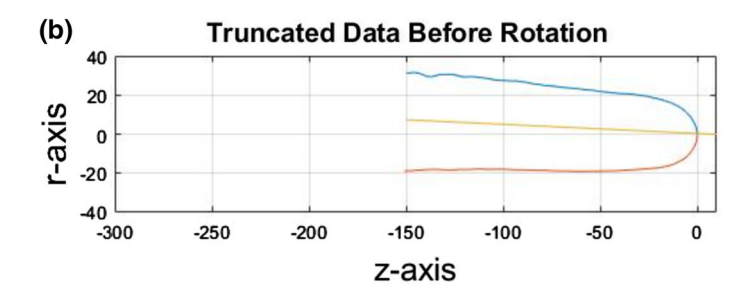
9 Appendix B: Experimental protocols and image processing

Physcomitrella patens tissue was cultured using standard methods according to [21]. For imaging, one-week old moss tissue was transferred to a microscope preparation equipped with an agar pad as described in [33]. To stain the cell walls, before sealing the preparation, $30 \mu l$ of calcofluor-white (final concentration $10 \mu g/ml$) were pipetted on the plants. Cells were imaged with an inverted epifluorescence microscope Axiovert 200M (Zeiss) with a 20X lens (NA = 0.3); the calcofluor-white signal was imaged with a DAPI filter. After image acquisition, to obtain the outline of the cells we used the imageJ plugin "J Filament" [34]. The plugin outputs the z, r coordinates of each point of the cells outline.

Two cell outlines may have different orientations, and we need to rotate all the cell outlines in order to register them along the same long axis. We develop the following optimization problem to identify the orientation of the long axis and rotate the cell outlines accordingly. For each coordinate dataset $C := \vec{r}_i = (z_i, r_i)$, for $i \in \{1, 2, \dots, N\}$ for a cell outline (shown in Fig. 10a), we have looked for the line ar+z+c=0 which minimize the sum of squares of distances from all the coordinates to the line $\sum_{i=1}^N (ar_i+z_i+c)^2/(a^2+1)$ (See the orange line in Fig. 10b). We then rotate all the coordinates by the same angle between the line which we found and the horizontal axis, using the tip point as the reference (See the juncture of the red and blue curves in Fig. 10b). After the rotation (Fig. 10c), if the new tip point (the point farthest to the right) is no longer the original tip point, we take the new tip point as the tip point. All cell outlines are put together by overlapping the tip points. Finally, we reflect the lower half of the cell outline above the horizontal axis. For readers who are interested in using our methodology, we have shared the code at https://github.com/DanukGOAT/Cell-Wall-Tension-Inference with written tutorial and input data samples. This pipeline computes and plots rotated cell outlines (as in Fig. 9a, c) and tension distributions (as in Fig. 9b, d) from the list of cell outline coordinates generated from imageJ plugin "J Filament".







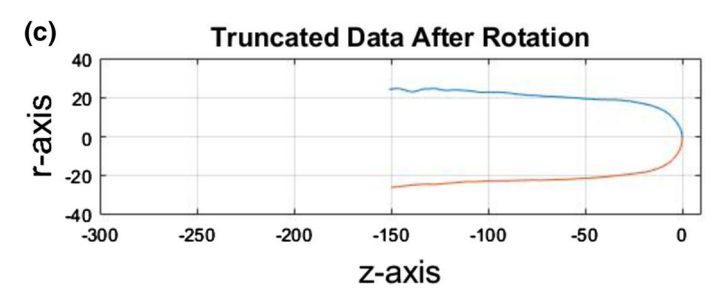


Fig. 10 Image processing of one single cell outline. **a** A typical cell outline obtained from imageJ plugin "J Filament" [34]. The plugin outputs the z, r coordinates of each point of the cells outline. **b** The truncated cell outline for $N_m=160$ points from the tip point for both upper (blue) and lower (red) cell outline branches, respectively. The major axis (orange) is identified from the optimization (see text). **c** The truncated cell outline after registering the direction of the orange major axis in **b** as the new z-axis. The r- and z-axes are rescaled by $0.315 \,\mu m$

References

- 1. A. Goriely, M. Tabor, Phys. Rev. Lett. 90, 108101 (2003)
- 2. J. Dumais, S.L. Shaw, C.R. Steele, S.R. Long, P.M. Ray, Int. J. Dev. Biol. 50, 209 (2006)
- 3. O. Campas, L. Mahadevan, Curr. Biol. 19, 2102 (2009)
- 4. P. Fayant, O. Girlanda, Y. Chebli, C.-É. Aubin, I. Villemure, A. Geitmann, Plant Cell 22, 2579 (2010)
- 5. E.R. Rojas, S. Hotton, J. Dumais, Biophys. J. 101, 1844 (2011)
- J.F. Abenza, E. Couturier, J. Dodgson, J. Dickmann, A. Chessel, J. Dumais, R.E.C. Salas, Nat. Commun. 6, 1 (2015)
- V. DavÍ, L. Chevalier, H. Guo, H. Tanimoto, K. Barrett, E. Couturier, A. Boudaoud, N. Minc, Proc. Natl. Acad. Sci. 116, 13833 (2019)
- 8. R. Dyson, O. Jensen, J. Fluid Mech. 655, 472 (2010)
- 9. Z. Hejnowicz, B. Heinemann, A. Sievers, Z. Pflanzenphysiol. 81, 409 (1977)
- 10. J. Dumais, S.R. Long, S.L. Shaw, Plant Physiol. 136, 3266 (2004)



- A. Goriely, M. Tabor, and A. Tongen, in *IUTAM Symposium on Cellular, Molecular and Tissue Mechanics* (Springer, 2010), pp. 245–255
- 12. O. Ali, V. Mirabet, C. Godin, J. Traas, Ann. Rev. Cell Dev. Biol. 30, 59 (2014)
- 13. O. Campàs, E. Rojas, J. Dumais, L. Mahadevan, Am. J. Bot. 99, 1577 (2012)
- 14. R.E. Williamson, Funct. Plant Biol. 17, 601 (1990)
- O. Hamant, M.G. Heisler, H. Jönsson, P. Krupinski, M. Uyttewaal, P. Bokov, F. Corson, P. Sahlin, A. Boudaoud, E.M. Meyerowitz et al., Science 322, 1650 (2008)
- 16. B. Bozorg, P. Krupinski, H. Jönsson, PLoS Comput. Biol. 10, e1003410 (2014)
- A. Sampathkumar, P. Krupinski, R. Wightman, P. Milani, A. Berquand, A. Boudaoud, O. Hamant, H. Jönsson, E.M. Meyerowitz, elife 3, e01967 (2014)
- N. Hervieux, M. Dumond, A. Sapala, A.-L. Routier-Kierzkowska, D. Kierzkowski, A.H. Roeder, R.S. Smith, A. Boudaoud, O. Hamant, Curr. Biol. 26, 1019 (2016)
- 19. A. Sampathkumar, A. Yan, P. Krupinski, E.M. Meyerowitz, Curr. Biol. 24, R475 (2014)
- H. Oliveri, J. Traas, C. Godin, O. Ali, J. Math. Biol. 78, 625 (2019)
- 21. F. Furt, Y.-C. Liu, J.P. Bibeau, E. Tüzel, L. Vidali, Plant J. 73, 417 (2013)
- 22. B. Menand, G. Calder, L. Dolan, J. Exp. Bot. 58, 1843 (2007)
- 23. R. Benkert, G. Obermeyer, F.-W. Bentrup, Protoplasma 198, 1 (1997)
- 24. G. Gierz, S. Bartnicki-Garcia, J. Theor. Biol. 208, 151 (2001)
- 25. P.K. Hepler, L. Vidali, A.Y. Cheung, Ann Rev. Cell Dev. Biol. 17, 159 (2001)
- 26. R.A. Cole, J.E. Fowler, Curr. Opin. Plant Biol. 9, 579 (2006)
- 27. S.H. Tindemans, N. Kern, B.M. Mulder, J. Theor. Biol. 238, 937 (2006)
- 28. L. Zonia, T. Munnik, J. Exp. Bot. 59, 861 (2008)
- J. Wessels, P. Mol, J. Sietsma, C. Vermeulen, in: Biochemistry of Cell Walls and Membranes in Fungi (Springer, 1990) pp. 81–95
- C. Pozrikidis et al., Boundary Integral and Singularity Methods for Linearized Viscous Flow (Cambridge University Press, Cambridge, 1992)
- 31. M. Wu, M. Ben Amar, Math. Mech. Solids **20**, 663 (2015)
- 32. M. Wu, M. Ben Amar, Biomech. Model. Mechanobiol. 14, 357 (2015)
- 33. G. Galotto, J.P. Bibeau, L. Vidali, Plant Cell Morphogenesis (Springer, Berlin, 2019), pp. 307–322
- 34. M.B. Smith, H. Li, T. Shen, X. Huang, E. Yusuf, D. Vavylonis, Cytoskeleton 67, 693 (2010)

